

1 **Rare Earth Elements (REE)-minerals in the Silius fluorite vein system**  
2 **(Sardinia, Italy)**

3  
4  
5  
6  
7  
8  
9 Mondillo N.<sup>1,2\*</sup>, Boni M.<sup>1</sup>, Balassone G.<sup>1</sup>, Spoleto S.<sup>1</sup>, Stellato F.<sup>1</sup>,  
10 Marino A.<sup>3</sup>, Santoro L.<sup>2</sup>, Spratt J.<sup>2</sup>

11  
12  
13 <sup>1</sup> *Dipartimento di Scienze della Terra, dell'Ambiente e delle Risorse, Università degli Studi di Napoli*  
14 *Federico II, via Mezzocannone 8, 80134, Napoli Italy*

15 <sup>2</sup> *Department of Earth Sciences, Natural History Museum, Cromwell Road, SW7 5BD, London UK*

16 <sup>3</sup> *Fluorite di Silius S.p.A. Viale Merello 14, 09023, Cagliari Italy*

17  
18  
19  
20  
21  
22 \*Corresponding author: [nicola.mondillo@unina.it](mailto:nicola.mondillo@unina.it)

23

24

25 ABSTRACT

26

27 The Silius vein system located in SE Sardinia (Italy) is analogous to other late- to post-Hercynian  
28 mineralization of this type in Europe. The system consists of two main veins, characterized by  
29 various generations of fluorite, calcite and quartz, with initial ribbon-like geometries, followed by  
30 breccias and cockade-like encrustations. In this study, aimed at investigating the REE concentrations  
31 in the Silius vein system, average REE amounts around 800 ppm (locally over 1500 ppm  $\Sigma$ REE),  
32 related to the presence of the REE-bearing minerals synchysite-(Ce) and xenotime-(Y), were detected  
33 in the carbonate gangue of the fluorite orebody. From the geochemical characteristics of these  
34 minerals, and the textural relationships with other gangue phases, it is likely that synchysite-(Ce) and  
35 xenotime-(Y) formed at the same P-T-X conditions as the other minerals of the Silius fluorite  
36 mineralization. Synchysite-(Ce) and xenotime-(Y) at Silius could be related to a local circulation  
37 phenomenon, where the REE are derived from a REE-bearing source rock in the basement of  
38 southeastern Sardinia, which has been leached by the same fluids precipitating the fluorite/calcite  
39 mineralization. REE minerals could possibly be found elsewhere in association with the carbonate  
40 gangue of still unexploited parts of fluorite hydrothermal vein deposits, as well as in dumps and  
41 tailings accumulated during fluorite processing.

42

43 *Keywords: SE Sardinia, hydrothermal veins, REE, fluorite, REE-minerals, carbonates*

44

45

## 46 **1. Introduction**

47

48 Rare Earth Element (REE)-bearing minerals occur in many igneous, sedimentary, and metamorphic  
49 rocks, where they may be concentrated in ore deposits both related to igneous and hydrothermal  
50 processes, or associated with sedimentary environments and weathering (Chakhmouradian and Wall,  
51 2012). REE-rich ores in carbonatites and peralkaline igneous rocks can be directly derived from  
52 magmatic processes, but also from metasomatism and hydrothermal remobilization of magmatic REE  
53 minerals (Chakhmouradian and Zaitsev, 2012; Gysi and Williams-Jones, 2013). Other REE-bearing  
54 mineral deposits can be associated with hydrothermal quartz- and fluorite-bearing veins of  
55 orthomagmatic derivation (Samson et al., 2004; Williams-Jones et al., 2000). Typical weathering-  
56 related REE-mineral concentrations occur in placers, and in laterite and ion-absorption clay deposits  
57 (Chakhmouradian and Wall, 2012).

58 REE concentrations have been also detected in several fluorite vein systems, not directly related to  
59 magmatism, occurring in the Hercynian basement of Europe. Hercynian fluorite vein systems were  
60 emplaced in the European basement between late Paleozoic and early Mesozoic, as a consequence of  
61 distal tectonics (e.g. continental extension) associated with the initial opening of the Atlantic Ocean,  
62 and circulation of brines within the basement (Muechez et al., 2005; Muñoz et al., 1999, 2005). To  
63 date, REE contents of these systems has largely focused on the Paleozoic-Mesozoic hydrothermal  
64 veins themselves, focused at defining their occurrence in fluorite, caused by ion-substitution  
65 processes (Dill et al., 2011; Möller, 1991; Möller et al., 1976, 1994; Möller and Giese, 1997;  
66 Schwinn and Markl, 2005). Several studies, carried out on fluorite veins in south Germany (e.g. Harz  
67 Mountains, Schwarzwald, Bohemian Massif), revealed that the measured REE concentrations are  
68 associated with the occurrence of specific REE minerals (e.g. Dill et al., 2011; Giere, 1996, and  
69 references therein; Haack et al., 1987; von Gehlen et al., 1986). Comparable research was also  
70 carried out on Triassic-Jurassic fluorite deposits in the Hercynian terrains of northern Africa  
71 (Bouabdellah et al., 2010; Cheilletz et al., 2010).

72 We present here the results of an investigation aimed at evaluating the REE behavior and  
73 fractionation in the Silius fluorite vein system, located in SE Sardinia, Italy. The Silius system is  
74 analogous to other late- to post-Hercynian mineralization of this type in Europe (Natale, 1969; Boni  
75 et al., 2009). Fluorite and galena reserves were evaluated at 2 million tons of raw material in 2006  
76 (Castorina et al., 2008), when mining operations ceased, but a new exploration campaign has been  
77 recently carried out, to find new fluorite resources. The REE contents in the Silius fluorite ore had  
78 been already reported by Castorina et al. (2008), in relation to a more general study on the different  
79 types of fluorite deposits in Sardinia. These authors used the REE content in fluorite to distinguish  
80 between the different hydrothermal F-ore deposits on the island, and compared their data with the  
81 REE contents of other Hercynian fluorite mineralizations in Europe.

82 As for other classical studies on European fluorite deposits (e.g. Dill et al., 2001), we have re-  
83 evaluated the REE amounts contained in both fluorite and host rock. Moreover, we have also carried  
84 out a thorough mineralogical research on the various gangue components of the vein system. The  
85 results of this study, aside from obtaining new data on the nature of the REE minerals in the Silius  
86 veins, have shed new light on the characteristics of this kind of fluorite ore and its gangue.

87

## 88 **2. Geological Setting**

89

### 90 *2.1. Regional Geology*

91

92 The Sardinia-Corsica Paleozoic basement represents a fragment of the Hercynian orogen (Arthaud  
93 and Matte, 1977; Carmignani et al., 1994; Crowley et al., 2000) that can be subdivided into three  
94 tectono-metamorphic zones (Fig. 1A): i) a “foreland zone”, outcropping in southwestern Sardinia,  
95 with low-grade or no metamorphism, ii) a “nappe-zone”, in southeastern and central parts of Sardinia,  
96 affected by low- to medium-grade metamorphism, and iii) an “inner zone”, in northern Sardinia,  
97 characterized by medium- to high-grade metamorphic signatures (Carmignani et al., 2001).

98 The “external zone” successions (SW Sardinia), spanning in age from early Cambrian to Devonian  
99 and Carboniferous, are represented by clastic and carbonate, mainly shallow water sedimentary rocks  
100 (Bechstädt and Boni, 1994; Carmignani et al., 2001).

101 The “nappe-zone” area, where the Silius mineralization is located, is characterized by various  
102 lithotypes (Fig. 1B). The upper Cambrian-Ordovician successions mostly consist of siliciclastics  
103 (metasandstones, phyllites and quartzites), collectively grouped in the “Arenarie di San Vito” (Fig.  
104 1B) and “Solanas” Formations (not outcropping in the study area). These Formations are overlain by  
105 the so-called “Ordovician magmatic and volcano-sedimentary complex” (Carmignani et al., 2001),  
106 which consists of both effusive and intrusive igneous products, displaying an almost complete arc-  
107 related calc-alkaline suite of middle to late Ordovician age (Oggiano et al., 2010; Gaggero et al.,  
108 2012). In the Silius area the Ordovician volcano-sedimentary complex, named “Porfiroidi” Formation  
109 (Fig. 1B), is represented by rare andesitic lavas and abundant metasediments derived from the  
110 reworking of the former, overlain by metarhyolites and metarhyodacites (Carmignani et al., 1994).  
111 The Ordovician magmatic and volcano-sedimentary complex is unconformably overlain by  
112 siliciclastic continental to neritic sediments, which were deposited during a period of active intraplate  
113 magmatism, resulting in alkali basalt flows, sills and dykes (late Ordovician-Silurian) (Oggiano et al.,  
114 2010; Gaggero et al., 2012) (Fig. 1B). In the Silurian to Devonian period, the magmatic activity  
115 stopped and pelagic sediments (Graptolitic Shales, or “Formazione degli Scisti a Graptoliti”) were  
116 deposited (Fig. 1B). These consist of black shales and pelagic limestones, and are interrupted at the  
117 top by the Carboniferous (Culm-type) flysch (Carmignani et al., 2001).

118 The “inner zone” is represented by a high-grade metamorphic complex, mainly consisting of  
119 amphibolites, which are southward bounded by an eclogite-bearing belt, interpreted as the suture  
120 zone of the Hercynian orogen (Carmignani et al., 1994).

121 The Hercynian compressive deformation was concluded by the emplacement of granite batholiths  
122 that occurred during the extensional period associated with the collapse of the orogen (310-280 Ma;  
123 Di Vincenzo et al., 1994; Carmignani et al., 2001). The entire basement was later intruded by

124 Permian to Triassic magmatic dykes of bimodal composition (Ghezzo and Orsini, 1982; Atzori and  
125 Traversa, 1986; Carmignani et al., 2001). During this period, several hydrothermal vein systems  
126 containing fluorite, barite and sulfides were developed in SE Sardinia. The Silius mineralization  
127 corresponds to one of these vein systems (Natale, 1969). Other post-Hercynian occurrences in the  
128 area are set within cataclastic and mylonitic belts, as the so-called “*Filone Argentifero del Sarrabus*”,  
129 a complex association of stockworks and veins of Pb-Cu-sulfides and silver minerals, as well as the  
130 stibnite ( $\pm$ scheelite) vein systems of Su Suergiu and Corti Rosas (Valera et al., 1974; Belkin et al.,  
131 1984; Carmignani et al., 1978).

132

## 133 2.2. *The Silius hydrothermal veins*

134

135 The Silius vein system (Fig. 1B) crops out discontinuously for 2-3 km along a NE-SW strike,  
136 between the Acqua Frida area (39°30'46"N-9°15'05"E), the Muscadroxiu shaft (39°31'00"N-  
137 9°15'18"E) and the Genna Tres Montis shaft (39°31'38"N-9°16'00"E), at an elevation ranging  
138 between 600 and 700 m a.s.l. At the 400 m level, the veins reach a maximum length of 4 km.

139 The system consists of two main veins, called “San Giorgio” and “San Giuseppe” (Fig. 2A), which  
140 have an almost vertical dip (about 75°), and a strike of N045E along the main sector Acqua Frida -  
141 Genna Tres Montis, and N065E northeastward from Genna Tres Montis. These two veins are almost  
142 parallel in the topmost levels, with a spacing of 70 m on average, but they coalesce at a depth of 350  
143 m a.s.l. in the NE sector, and at a depth of 450 m a.s.l. in the SW sector of the mineralized area. The  
144 San Giorgio vein was the first to be formed, and was displaced and brecciated by the San Giuseppe  
145 vein. The San Giorgio vein contains bands of chalcedony, pink fluorite, barite and calcite. The San  
146 Giuseppe vein is also banded, and shows several generations of fluorite, calcite and galena (Fig. 2A,  
147 B, C). The width of the veins ranges between 7-8 m in outcrop and 15-20 m in depth, where they are  
148 interconnected (Fig. 2B). The Silius vein system has been mined from the surface (around 600 m  
149 a.s.l.) down to 200 m a.s.l., and explored to 100 m a.s.l. The upper part of the vein system contains

150 fluorite, barite and galena with grades of 35%, 10% and 3%, respectively, whereas in the lower zones  
151 the amount of barite decreases, and the fluorite and galena grades can also reach 50% and 6%,  
152 respectively. Quartz and carbonates are the main constituents of the gangue. Two less economically  
153 important veins (called San Giovanni and Davide) are also parallel to the other veins, and can be  
154 traced to the 500 m level.

155 All the veins are mainly hosted by the “Porfiroidi” Formation and rarely by Late Ordovician  
156 sedimentary rocks of the Graptolitic Shales Formation. The fluorite-barite mineralized veins cut  
157 locally the late- to post-Hercynian (Permian to Triassic acid and basic-intermediate) magmatic dykes:  
158 this relationship defines a relative minimum age for the mineralization process (Natale, 1969). The  
159 veins are characterized by successive generations of fluorite, calcite and quartz, with initial ribbon-  
160 shaped geometries, followed by breccias and cockade-like textures (Fig. 2D). The different  
161 generations are always accompanied by sulfides (marcasite, sphalerite and galena), and in the late  
162 stages by barite (Natale, 1969).

163 In previous fluid inclusion studies on the Silius mineralization, it was reported that most ore minerals  
164 precipitated at temperatures in the range of 120-180 °C from fluids with salinities reaching up to ~18  
165 wt.% NaCl equiv. (Boni et al., 2009). Due to the very low first melting temperatures (~ -50 °C)  
166 recorded in both fluorite and calcite, the authors suggested the involvement of Ca-rich fluids in the  
167 mineralization process. Lead isotopes of sulfides in the Silius mineralization have been determined as  
168 intermediate between the compositions of Ordovician metavolcanic rocks (“Porfiroidi” Formation)  
169 and Hercynian granites (Boni et al., 2009). Sr and Nd isotopes of Silius fluorite, measured by  
170 Castorina et al. (2008), have a signature coherent with a brine circulation within both Paleozoic  
171 metasedimentary rocks and Hercynian granitoids.

172

### 173 **3. Sampling and analytical methods**

174

175 The samples analyzed in this study were mainly collected in both the San Giuseppe and the San  
176 Giorgio veins, along the two vertical sections of the Muscadroxiu and the Central shafts of the mine  
177 (the latter is located between the Muscadroxiu and the Genna Tres Montis shafts) at every 20 m, from  
178 100 m a.s.l. up to 200 m a.s.l. At each sampling site, we collected fluorite, calcite, and fragments of  
179 the host rock. Additional sampling was carried out at the Acqua Frida shaft, at 300 m elevation,  
180 where we collected fluorite and calcite from both veins. In Table A1 are listed all the analyzed  
181 samples.

182 Fluorite and calcite were cleaned of the impurities (sulfides and Fe-oxides) by handpicking under  
183 binocular microscope. The purity of the minerals was tested with X-ray diffraction analysis, by using  
184 a Seifert–GE ID3003 diffractometer (Dipartimento di Scienze della Terra, dell’Ambiente e delle  
185 Risorse, Università degli Studi di Napoli Federico II), with CuK $\alpha$  radiation, Ni-filtered at 40 kV and  
186 30 mA, 3-80  $^{\circ}2\theta$  range, step scan 0.02 $^{\circ}$ , time 10 sec/step, and the RayfleX (GE) software package; a  
187 silicon wafer was used to check the instrumental setting. Sample holder was a zero-background plate  
188 of quartz crystal cut and polished 6 $^{\circ}$  of the *c*-axis.

189 For polished thin sections preparation, the samples were impregnated with Araldite D and Raku  
190 Hardener EH 2950 (OMT Laboratory, Aosta, Italy). Cathodoluminescence microscopy (CL) was  
191 carried out with a Hot Cathode Instrument at the Heidelberg University. Secondary electron  
192 imaging by scanning electron microscopy (SEM), and energy dispersion spectrometry (EDS)  
193 investigations on thin sections were carried out with a Jeol JSM 5310, equipped with the INCA X-  
194 stream pulse processor and the 4.08 version Inca software (Oxford Instruments detector) (DiSTAR,  
195 Università di Napoli, Italy), operating at 15 kV primary beam voltage, 50-100 mA filament current,  
196 variable spot size and 50 s net acquisition time. Reference standards were: albite (Si, Al, Na),  
197 orthoclase (K), wollastonite (Ca), diopside (Mg), almandine (Fe), rutile (Ti), barite (Ba), strontianite  
198 (Sr), eskolaite (Cr), rhodonite (Mn), pyrite (S), sphalerite (Zn), galena (Pb), fluorite (F), apatite (P),  
199 sylvite (Cl), smithsonian phosphates (La, Ce, Nd, Sm, Y), pure vanadium (V) and Cornig glass (Th,  
200 U). Analytical errors are 1% rel. for major elements and 3% rel. for minor elements.

201 Quantitative data sets of selected samples were obtained by wavelength dispersion spectrometry (full  
202 WDS), using a Cameca SX10050 electron microprobe operating at 20.5 kV, 20.5 nA, and 10  $\mu$  m  
203 spot size (Natural History Museum, London, UK). ~~All the compositions of the standards used~~  
204 ~~standard~~ are reported in Table A2. Interference corrections ~~were have been~~ carried out prior to matrix  
205 correction for the following elements: F (overlapping element, Ce), Nd (Ce), Sm (Ce), Ba (Pr) and La  
206 (Nd)Ti (Ba), Ce (Ba), U (K), Nd (Ce), Sm (Ce), Gd (La, Ce, Nd), Ce (La). A monazite (Manangotry)  
207 standard (composition and determinations in Table A32) was used as a quality control sample. WDS  
208 detection limits for each element are reported in Table 3, ~~and are mostly in the order of 0.01 wt%.~~

209 Major, minor and trace (REE) elements in fluorite, carbonate minerals and host rock samples have  
210 been measured at the ACME laboratories (Vancouver, Canada) and at the Activation Laboratories  
211 (Ancaster, Canada). In both the laboratories, the same protocol was adopted: the samples were  
212 pulverized to 85% -200 mesh, to obtain about 20 g of pulp. Major oxides and several minor elements  
213 were analyzed by ICP-OES following a LiBO<sub>2</sub>/Li<sub>2</sub>B<sub>4</sub>O<sub>7</sub> fusion and dilute nitric digestion. Loss on  
214 ignition (LOI) was calculated by weight difference after ignition at 1000°C. Rare earth and refractory  
215 elements were determined by ICP-MS following a LiBO<sub>2</sub>/Li<sub>2</sub>B<sub>4</sub>O<sub>7</sub> fusion and nitric acid digestion. In  
216 addition, a separate volume split was digested in *Aqua Regia* and analyzed by ICP-MS to detect the  
217 precious and base metals. Lower detection limits obtained in the two laboratories are reported in  
218 Tables 1, 2 and 4.

219

## 220 **4. Mineralogy and major element geochemistry**

221

### 222 *4.1. Fluorite*

223

224 The analyzed samples consist of medium-sized (<1cm) white/violet fluorite crystals, associated with  
225 calcite, quartz, barite and a few minute sulfide intergrowths. In thin section fluorite appears of  
226 different generations, each showing a strong blue luminescence under CL (Fig. 3). As reported in the

227 literature (Natale, 1969), it is possible to distinguish at least three fluorite generations: a first and  
228 more extensive generation consisting of fluorite alone (Fig. 3A, B), a second generation of fluorite  
229 with a calcite gangue (Fig. 3C, D), and a third one associated with quartz and barite (Fig. 3E, F).  
230 Minor amounts of SiO<sub>2</sub>, or various values of LOI or tot-C, detected by bulk chemical analyses (Table  
231 1), are related to intergrown quartz or carbonate minerals in fluorite, also revealed by XRD. The most  
232 contaminated samples have not been considered when discussing the relationships between REE  
233 sorption processes and genetic conditions.

234

#### 235 *4.2. Calcite and dolomite*

236

237 Mineralogical analyses have been conducted on several samples of the carbonate gangue, in order to  
238 verify if this consisted solely of calcite, as reported in the literature. X-ray diffraction clearly confirm  
239 that the carbonates of both the San Giorgio and San Giuseppe veins consist of a mixture of calcite  
240 and dolomite/ferroan dolomite, not yet reported for this vein system. The carbonate gangue can  
241 locally contain also small radial aggregates of newly formed kaolinite and quartz.

242 Calcite has yellow-orange colors under CL (Fig. 3D), and generally appears zoned. This indicates  
243 that variable amounts of Mn<sup>2+</sup> have substituted for Ca<sup>2+</sup> in the calcite lattice (Götze, 2012). Under  
244 microscopic observation, dolomite replaces calcite in patches (Fig. 3D). Replacive dolomite shows an  
245 extremely low luminescence under CL and consequently, when associated with calcite, it appears  
246 generally dark (Fig. 3D, F). Where the replacement is strongly pervasive, the dolomite colors under  
247 CL are dark-reddish. According to Götze (2012), the red CL color of dolomite is generally due to  
248 variable amounts of Mn<sup>2+</sup> ↔ Mg<sup>2+</sup> substitution in its structure. The low luminescence intensity of the  
249 Silius dolomite is related to the presence of discrete Fe<sup>2+</sup> amounts in the cationic sites, which quench  
250 the luminescence effects related to Mn<sup>2+</sup> (Götze, 2012).

251 SEM analyses confirmed that dolomite is not pure, but rather consists of the ferroan variety and  
252 ankerite, with Fe contents up to 23 wt.% FeO, and Mn up to 4 wt.% MnO (Fig. 4). Fe-bearing

253 dolomite has a mottled texture (Fig. 4A). Two replacive generations have been detected: an initial  
254 almost pure dolomite phase (<5 wt.% FeO, ~1 wt.% MnO), which is followed by a high-Fe dolomite  
255 phase (>6 wt.% FeO, >1 wt.% MnO) and eventually by ankerite (Fig. 4B, C).

256 Plotted on a diagram defined by  $\text{CaMg}(\text{CO}_3)_2$ - $\text{CaFe}(\text{CO}_3)_2$ - $\text{CaMn}(\text{CO}_3)_2$  (Fig. 5), the analyzed phases  
257 have a composition covering the field between pure dolomite and ferroan dolomite, with an almost  
258 continuous substitution between  $\text{Ca}_{1.08}\text{Mg}_{0.86}\text{Fe}_{0.03}\text{Mn}_{0.03}(\text{CO}_3)_2$  and  $\text{Ca}_{1.03}\text{Mg}_{0.42}\text{Fe}_{0.46}\text{Mn}_{0.09}(\text{CO}_3)_2$ .  
259 Only two outlier data show a more definite ankeritic composition:  $\text{Ca}_{1.01}\text{Mg}_{0.19}\text{Fe}_{0.68}\text{Mn}_{0.12}(\text{CO}_3)_2$  and  
260  $\text{Ca}_{1.01}\text{Mg}_{0.14}\text{Fe}_{0.73}\text{Mn}_{0.13}(\text{CO}_3)_2$ .

261 Chemical analyses on the carbonate gangue corroborate the Fe-rich composition of the dolomite. In  
262 fact, several samples from the gangue of the fluorite mineralization (Table 2) contain variable Mg  
263 and Fe amounts, which result from the mixture of different phases, as calcite, dolomite, Fe-rich  
264 dolomite and ankerite. These samples have a very similar composition, though they were collected in  
265 different zones of the mine.

266

#### 267 4.3. REE-minerals

268

269 Abundant REE-minerals have been detected within the carbonate gangue of both Silius mineralized  
270 veins (Fig. 4C, D, E, F, G, H). The mineralogy of these phases is quite simple and is mostly  
271 represented by synchysite-(Ce) (Table 3), a Ca-REE-fluorcarbonate [ $\text{CaREE}(\text{CO}_3)_2\text{F}$ ], and by rare  
272 xenotime-(Y) ( $\text{YPO}_4$ ). These minerals have been observed only under electronic microscope, because  
273 their amounts is below (or very near to) the XRD detection limits adopted in this study (< 1 wt.%).

274 In the analyzed samples, synchysite-(Ce) occurs as acicular and tabular crystals (Fig. 4C, D), with an  
275 average size below 100  $\mu\text{m}$  (Fig. 4E, F). In detail, synchysite-(Ce) has been observed both as single  
276 crystals and as composite aggregates in two main locations: firstly within the dolomitized calcite and  
277 Fe-bearing dolomite (Fig. 4C, D), and secondly within quartz veinlets and in cavities occurring  
278 among the calcite and dolomite patches (Fig. 4E). In the first setting, synchysite-(Ce) is distributed

279 throughout the irregularly dolomitized carbonate gangue, while it is almost absent in unaltered calcite  
280 (Fig. 4D). When synchysite-(Ce) occurs in the quartz veinlets, it is paragenetically followed by the  
281 third fluorite generation (Fig. 4F, G). No REE minerals have been found as inclusions in the fluorite  
282 crystals of the main generation that have been selected for ICP analyses.

283 Table 3 shows the chemical composition of synchysite-(Ce). The total REE content is on average  
284 around 45-46 wt.%. The formula of synchysite-(Ce) has been built on the basis of  $(\text{CO}_3)_2\text{F}$  and 5  
285 negative charges, and is given in Table 3. The average synchysite-(Ce) formula is  
286  $\text{Ca}_{1.07}(\text{La}_{0.19}, \text{Ce}_{0.36}, \text{Pr}_{0.04}, \text{Nd}_{0.15}, \text{Sm}_{0.03}, \text{Gd}_{0.03}, \text{Y}_{0.13})(\text{CO}_3)_2\text{F}$ .

287 Xenotime-(Y), similarly to synchysite-(Ce), occurs as subhedral crystals filling cavities within calcite  
288 and dolomite (Fig. 4H). The few analyzed specimens (EDS) are characterized by Dy and Yb contents  
289 of ~3 wt.%.

290

## 291 **5. REE geochemistry**

292

### 293 *5.1. Fluorite*

294

295 Excluding the fluorite samples contaminated by intergrown gangue minerals, the REE amounts  
296 determined by ICP on bulk fluorite are solely related to REE diffused in its crystal structure. In fact,  
297 no discrete REE minerals have been detected within the analyzed fluorite crystals in contrast to the  
298 carbonate gangue.

299 The REE contents of the Silius fluorite (Table 1) have been normalized to the post-Archean  
300 Australian Shale (PAAS; Taylor and McLennan, 1985), in order to compare their distribution with  
301 that observed in other deposits of the same type. REE in Silius fluorite are generally lower than  
302 PAAS. It is possible to observe that the REE concentrations normalized to PAAS have a roof-shaped  
303 pattern, characterized by positive Eu and Y anomalies (Fig. 6A). The Eu anomaly is also reflected in  
304 the Eu/Eu\* ratio, which is always above 2, except in samples FL-06 and FL-11 (contaminated by

305 quartz and carbonates), and in FL-05 and FL-12, which have no contamination. The patterns are  
306 asymmetric, because the majority of the samples have HREE contents very near to PAAS, whereas  
307 the LREE are strongly depleted; in fact, several samples have a  $\text{La/Yb}_n$  ratio  $< 1$ . The sample FL-3 is  
308 the only not-contaminated specimen to have the MREE and HREE more enriched than PAAS, and  
309 the LREE more depleted than PAAS ( $\text{La/Yb}_n$  ratio  $\sim 0.03$ ). Other samples (FL-06, FL-09, FL-10) have  
310 a  $\text{La/Yb}_n$  ratio slightly  $> 1$ , which is too small to be considered as proof for LREE/HREE fractionation.  
311 Moreover, these samples are characterized by normalized MREE values, which are higher than the  
312 LREE and HREE values.

313

## 314 *5.2. Carbonates*

315

316 Significant amounts of REE-bearing mineral inclusions, trapped in calcite and dolomite, clearly  
317 influence the REE concentrations determined by ICP on the bulk samples of the carbonate gangue.  
318 However, the amounts of REE possibly hosted in the calcite and dolomite structure are lower than the  
319 WDS detection limits.

320 The bulk carbonate gangue is characterized by REE contents notably higher than those in fluorite,  
321 (Table 2); in two of the considered samples, the total REE amounts are over 1500 ppm. In the  
322 diagram of PAAS-normalized REE-contents (Fig. 6B), it is possible to notice that the average pattern  
323 is almost flat for the carbonate samples, with positive drops in the Eu and Y positions. In detail, the  
324 CA-08 sample is the only one where HREE are more enriched than LREE, and LREE are less  
325 abundant than PAAS. The other samples are characterized by an enrichment of both LREE and  
326 HREE alike ( $\text{La/Yb}_n$  ratios around 1), or by a LREE enrichment higher than HREE ( $\text{La/Yb}_n$  ratios are  
327 around 2; only the sample CA-06 has a  $\text{La/Yb}_n$  ratio slightly  $> 4$ ). The Eu positive anomaly is marked  
328 by  $\text{Eu/Eu}^*$  ratios between 1.3 and 2.92.

329

## 330 *5.3. Vein system host rocks*

331

332 Two measured samples from the “Porfiroidi” Formation, which is the main host rock of the Silius  
333 deposit, have a REE content around 100 ppm  $\Sigma$ REE (Table 4). One of these samples, P6 is clearly  
334 contaminated with fluorite. Among the other types of host rocks, the highest REE contents have been  
335 detected in the samples consisting of late-Hercynian porphyritic dykes, whereas the metasedimentary  
336 black shales have very low REE values. All the host rocks have PAAS-normalized REE patterns  
337 depleted in REE, in comparison to the adopted reference (Fig. 6C). Only a sample of basic-  
338 intermediate porphyry has REE concentrations that are on average higher than PAAS. In general, two  
339 types of patterns can be observed: flat patterns and LREE-slightly depleted patterns ( $La/Yb_n < 1$ ). All  
340 of them do not show spikes or anomalies, either positive or negative. This behavior is different from  
341 that of fluorite, which has roof-shaped patterns with Eu and Y positive anomalies, and from the  
342 carbonate gangue, which is generally characterized by  $La/Yb_n$  ratios  $> 1$  and by Eu and Y positive  
343 anomalies (Fig. 6).

344

## 345 **5. Discussion**

346

347 *5.1. New insights on the mineralogy of the Silius vein system: are REE-bearing minerals compatible*  
348 *with this mineralization type?*

349

350 In the previously published studies on the Silius mineralization (Natale, 1969; Castorina et al., 2008;  
351 Boni et al., 2009), the deposit was described as a simple association of fluorite, barite, and mixed  
352 sulfides in a gangue consisting of calcite and quartz. The dolomite-ankerite phases detected in the  
353 present study are paragenetically younger than the other minerals of the veins because they replace  
354 earlier calcite. This event was then followed by, or is partly contemporaneous with a minor fluorite-  
355 barite-quartz mineralization stage, and by the precipitation of a late calcite phase. Consequently, the  
356 formation of both dolomite and Fe-dolomite can be considered as evidence for a short and abrupt

357 change in the chemical composition of the mineralizing fluids, which were temporarily enriched in  
358 Mg and Fe, in order to dolomitize the previously deposited calcite in both San Giorgio and San  
359 Giuseppe veins. The occurrence of synchysite-(Ce) and xenotime-(Y), that are paragenetically  
360 associated with dolomitized calcite, also marks a sharp temporary change in the chemistry of the  
361 fluids that for a while became REE-bearing.

362 Synchysite (the main REE-carrier in the Silius fluorite veins) is generally associated with  
363 orthomagmatic-hydrothermal or hydrothermal-metasomatic REE-mineralizations, but it has been also  
364 found in Alpine-type veins (Augé et al., 2014; Chakhmouradian and Wall, 2012; Föster, 2001; Giere,  
365 1996, and references therein; Williams-Jones et al., 2000). This mineral was detected in post-  
366 Hercynian veins in Germany (e.g. Harz Mountains, and Schwarzwald), where it is associated with  
367 bastnäsite (Giere, 1996, and references therein; Haack et al., 1987; von Gehlen et al., 1986). Small  
368 occurrences of synchysite-(Ce) in Sardinia are only recorded in association with molybdenite within  
369 Hercynian leucogranites in the small prospects of Su Senargiu (Sarroch) and Perda Pibera  
370 (Gonnosfanadiga) (Brizzi et al., 1994; Stara et al., 1996; Boni et al., 2003; Orlandi et al., 2013).

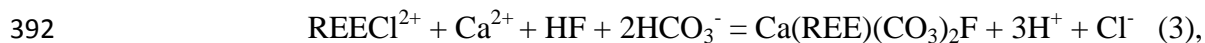
371 In hydrothermal environments REE are transported mainly as non-fluoride complexes (e.g. chloride  
372 species) in fluorine-bearing solutions (Williams-Jones et al., 2012; Migdisov and Williams-Jones,  
373 2014). These authors proposed a model in which fluoride ions would work as a binding ligand that  
374 promotes REE mineral deposition, rather than as an agent for REE transport. With this background,  
375 the co-genetic association of REE minerals and fluorite would be explained by the low solubility of  
376 both fluorite and REE minerals. Then, the ore-forming hydrothermal fluids carry appreciable  
377 concentrations of REE (and fluorine in the form of HF) in relatively acid conditions. The REE  
378 deposition may occur when the neutralization of the acidity of the solution induces the precipitation  
379 of fluoride-bearing minerals that in this model are represented only by bastnäsite. This happens, for  
380 example, when fluids interact with carbonate host rocks (e.g. dolomite or limestone), which buffer  
381 the pH to higher values, leading to the precipitation of the REE fluorocarbonate bastnäsite, according  
382 to the following reaction (Williams-Jones et al., 2012):



384 Any mechanism that produces an increase in pH and/or  $\text{HCO}_3^-$  activity, or a decrease in  $\text{Cl}^-$  activity  
385 will lead to the deposition of this mineral. If the host rock of the mineralization consists of dolomite,  
386 the ore fluid will react with the carbonate, providing an effective mechanism to precipitate the ore  
387 minerals (Williams-Jones et al., 2012):



389 This reaction produces a sharp increase in both pH and  $\text{HCO}_3^-$  activity. Concerning synchysite-(Ce),  
390 we may propose, by analogy with bastnäsite, a possible reaction for its formation based on the  
391 chemical reaction (1):



393 where the acid solution is buffered as in reaction (2).

394 Xenotime is a common accessory phase in granites and pegmatites, and is a common detrital mineral  
395 in siliciclastic sedimentary rocks; however, it may also form during hydrothermal processes (Brown  
396 et al., 2002; Kositcin et al., 2003; Schaltegger et al., 2005; Cook et al., 2013). In Sardinia,  
397 hydrothermal xenotime was found in the same leucogranite-hosted, molybdenite-related vein  
398 occurrences of Su Senargiu and Perda Pibera (Orlandi et al., 2013, 2014). In the Silius paragenesis,  
399 xenotime-(Y) has been detected as a phase strictly associated with synchysite-(Ce). Considering that  
400 synchysite preferentially hosts LREE, whereas xenotime is the common HREE carrier, this is  
401 probably a consequence of the different fractionation of LREE and HREE between the two minerals  
402 from the REE-bearing hydrothermal fluid. Gysi et al. (2015) investigated experimentally the  
403 thermodynamic properties of xenotime-(Y) and other HREE phosphates in a hydrothermal  
404 environment, and in aqueous  $\text{HClO}_4\text{-H}_3\text{PO}_4$  solutions, at temperatures up to 250 °C. From these  
405 experiments, the authors obtained that the solubility of HREE phosphate solids increases sharply with  
406 decreasing temperature. At Silius, most of the ore minerals precipitated at temperatures in the range  
407 of 120-180°C from a dominant fluid consisting of a  $\text{NaCl} \pm \text{CaCl}_2$ -rich brine (Boni et al., 2009).  
408 Hence, we may assume that the mineralizing fluid that precipitated xenotime-(Y), together with

409 synchysite-(Ce), can be similar to the model of Gysi et al. (2015) for xenotime-(Y) precipitation from  
410  $\text{H}_3\text{PO}_4\text{-HCl-HF}$ -fluid at 150 °C temperature. In these experimental conditions, xenotime is stable in  
411 the entire pH range that is higher than ~2. This wide stability range can be also compatible with the  
412 conditions of precipitation of Ca-bearing REE phases, which, as previously reported, are conditioned  
413 by the buffering reactions between the acid REE-bearing fluids and the carbonate host rock  
414 (Williams-Jones et al., 2012).

415 The occurrence of both synchysite-(Ce) and xenotime-(Y) at Silius is compatible with the genetic  
416 environment and the temperatures determined in previous studies by Castorina et al. (2008) and Boni  
417 et al. (2009).

418

#### 419 *5.2. Geochemistry of fluorite and gangue minerals: a comparison with previous studies*

420

421 The REE occurrence in fluorite has been largely sought in the Paleozoic-Mesozoic hydrothermal  
422 veins of Europe, as a way to investigate their genesis (e.g., Möller, 1991; Möller et al., 1976, 1994;  
423 Schwinn and Markl, 2005; Dill et al., 2011). It is well known that REE are hosted in the fluorite  
424 structure due to ion-substitution processes (Möller et al., 1998):



428 Möller et al. (1998) also suggested that Eu, Ce and Y anomalies in fluorite REE-PAAS-normalized  
429 patterns depend on the environmental conditions (mainly T) during the precipitation of this mineral.

430 In particular, the presence of Eu anomalies is strongly temperature-dependent, because at  
431 temperatures > 200 °C,  $\text{Eu}^{3+}$  is reduced to  $\text{Eu}^{2+}$ , which is very mobile and difficult to be incorporated  
432 into the fluorite structure, and therefore tends to remain in the fluid. This produces negative Eu  
433 anomalies in fluorites precipitated from a fluid with  $T > 200$  °C. Instead, a Eu anomaly is lacking or  
434 slightly positive in fluorite precipitated from a fluid with a temperature < 200 °C (Möller et al., 1998).

435 Another possibility is that the Eu anomaly was inherited from the REE source rock (Schwinn and  
436 Markl, 2005). Silius fluorite shows a clear positive Eu anomaly, which probably indicates  
437 precipitation temperatures < 200 °C, in agreement with the homogenization temperatures of the fluid  
438 inclusions measured by Boni et al. (2009).

439 The presence or absence of a cerium anomaly is controlled by the oxygen fugacity of the fluid, which  
440 controls the redox reaction between  $Ce^{3+}$  and  $Ce^{4+}$ .  $Ce^{4+}$  does not migrate in the fluid together with  
441 other REE, because it is typically retained in Fe and Mn-hydroxides (Möller and Bau, 1993). The  
442 absence of Ce anomalies in the REE patterns of Silius fluorite confirms that the fluids precipitating  
443 the main fluorite generation were relatively oxygen-poor, a fact that is also confirmed by the  
444 presence of sulfides (galena and pyrite > sphalerite) associated with fluorite.

445 Bau and Dulski (1995) suggested that the Y/Ho ratio varies during the migration of the hydrothermal  
446 fluid through the rocks: in particular, a progressive migration of the fluids produces a negative  
447 correlation between the Y/Ho ratio and the La/Ho ratio. If we exclude from the discussion the fluorite  
448 samples FL-04, FL-06 and FL-11 (Table 1) clearly contaminated by other minerals (quartz, barite,  
449 calcite), it appears that the Silius fluorite is characterized by a positive correlation between the La/Ho  
450 and Y/Ho ratios (Fig. 7). This would exclude a prolonged migration through the host rock before  
451 fluorite precipitation, though PAAS-normalized patterns showing positive Y anomalies (as in this  
452 case) generally form when the distance between the sites of REE mobilization and deposition is big  
453 (Bau and Dulski, 1995).

454 REE geochemistry of carbonates in Hercynian fluorite veins has been widely investigated, for  
455 example in the deposits of the Harz mountains in Germany (e.g. Möller et al., 1984), in the small  
456 occurrences of the Valle de Tena in Spain (Subías and Fernández-Nieto, 1995), and in the El  
457 Hammam orebodies in Morocco (Cheillez et al., 2010). More specifically, the REE occurrence in the  
458 structure of carbonate minerals, i.e. calcite, siderite, and magnesite, has been described by Bau and  
459 Möller (1992) for the German ores. However, in our case study, it is necessary to consider that the  
460 REE amounts in the carbonates are mostly related to the occurrence of interspersed synchysite-(Ce)

461 and xenotime-(Y) mineral inclusions, and that they do not depend on substitution processes of REE  
462 within calcite or dolomite lattices. Consequently, it is challenging, for example, to explain why all  
463 REE patterns of the bulk carbonates at Silius are characterized by Eu positive anomalies, similarly to  
464 those of pure fluorite. In our opinion, the different possibilities accounting for the observed Eu  
465 positive anomaly are:

- 466 i) the Eu anomaly of the carbonate gangue depends on the physico-chemical conditions  
467 during precipitation of the minerals; after Bau and Möller (1992), a positive Eu anomaly  
468 in calcite indicates precipitation temperatures of at least 200-250 °C, reducing conditions,  
469 and Eu reduction to  $\text{Eu}^{2+}$ , which is easily incorporated into the calcite structure;
- 470 ii) the Eu positive anomaly in the carbonate gangue is inherited from the REE source rock:  
471 considering the high contribution of synchysite-(Ce) to the total REE concentration in the  
472 gangue, it is probable that the REE were not fractionated on the basis of their oxidation  
473 state when entering the mineral, but were incorporated *in toto* from the hydrothermal fluid,  
474 thus preserving the footprint of their original source. Considering also that fluorite and its  
475 carbonate gangue precipitated together, also the Eu positive anomaly in fluorite could be  
476 partly inherited from the REE source, not being only an effect of a temperature-dependent  
477 process.

478 Considering the geological, textural, and paragenetic characteristics of the Silius mineralization,  
479 option (i) is highly likely, but considering the high contribution of synchysite-(Ce) to the REE  
480 concentration in the bulk gangue, option (ii) can be also valid. Consequently, it is not possible to  
481 totally exclude that the Eu anomaly was inherited from the REE composition of an original source  
482 rocks. A comparison between the REE patterns of fluorite and carbonate gangue with those of several  
483 host rocks at Silius shows that both fluorite and carbonates have patterns completely different from  
484 those of their host rocks (Fig. 6). This point would be enough to exclude a provenance of the REE  
485 from the leaching of the same rocks hosting the vein system. The association of REE-fluorcarbonates  
486 with Fe-bearing dolomite and quartz may indicate that the hydrothermal fluids have leached Mg-Fe

487 silicatic rocks from the basement, which should have contained discrete REE amounts from the start.  
488 Moreover, the presence of a positive Eu anomaly in the normalized REE pattern of both fluorite and  
489 carbonates (if partly inherited from the original REE source), may suggest that the REE source was  
490 characterized by high feldspar (specifically plagioclase) contents. On this point, for example,  
491 Castorina et al. (2008), referring to the experimental work of Schwinn and Markl (2005), suggested a  
492 possible contribution of a gneiss-derived hydrothermal fluid to the formation of the Silius vein  
493 system. On the other hand, the upper Ordovician alkali basalts occurring in Southeastern Sardinia  
494 have many characteristics, which fit the above constraints and make these rocks a potential REE-  
495 source for the Silius mineralization. In fact, they are Mg-Fe rich, contain discrete amounts of REE,  
496 and also show positive Eu anomalies in the REE chondrite-normalized pattern (Gaggero et al. 2012).  
497 The occurrence of xenotime-(Y) at Silius suggests also the presence of phosphorus within the source  
498 rocks. Phosphorus could have been leached from the Silurian black shales and pelagic sediments of  
499 the Graptolitic Shales Formation, which locally host the fluorite mineralization.

500

## 501 **6. Conclusions**

502

503 This study has shown that REE concentrations in the carbonate gangue of the Silius fluorite deposit  
504 (SE Sardinia, Italy), are related to the presence of the REE-bearing minerals synchysite-(Ce) and  
505 xenotime-(Y). From the discussion of the data and the comparison with the existing literature, it is  
506 likely that both synchysite-(Ce) and xenotime-(Y) formed at the same P-T-X conditions considered  
507 for the other minerals of the Silius fluorite mineralization. Rare earth elements are likely derived  
508 from a REE-bearing source rock in the basement of southeastern Sardinia, which has been leached by  
509 the same fluids precipitating the fluorite/calcite mineralization.

510 In our opinion, the discovery of REE-minerals in the Silius fluorite mine may open interesting  
511 perspectives for the exploration of sub-economic REE concentrations in this type of deposits, where

512 REE could be recovered as by-product of the fluorite exploitation. Moreover, REE minerals could  
513 possibly be found also in dumps and tailings accumulated during the fluorite concentration process.

514

## 515 **Acknowledgments**

516

517 We would like to thank Ing. G. Mura, Director of the Silius mine, for having allowed us to sample in  
518 the underground levels, and R. de' Gennaro (DiSTAR, Napoli) for the SEM-EDS analyses. Thanks  
519 are also due to the anonymous reviewers, whose comments have highly enhanced the quality of the  
520 manuscript, and F. Pirajno for editorial handling. N. Mondillo would like to thank B. Lehmann, for  
521 the positive discussion on the Harz fluorite, and R. Herrington for suggestions and help. This work  
522 was partially financed by the Università degli Studi di Napoli Federico II, grant RDIP2014 to M.  
523 Boni and N. Mondillo.

524

## 525 **References**

526

527 Arthaud, F., Matte, P., 1977. Late-Palaeozoic strike-slip faulting in Southern Europe and Northern  
528 Africa: results of a right lateral shear zone between the Appalachians and the Urals. *Geol. Soc. Am.*  
529 *Bull.* 88, 305–1320.

530 Atzori, P., Traversa, G., 1986. Post-granitic Permo-Triassic dyke magmatism in eastern Sardinia  
531 (Sarrabus p.p., Barbagia, Mandrolisai, Goceano, Baronie and Gallura). *Per. Miner.* 55, 203–231.

532 Augé, T., Bailly, L., Wille, G., 2014. An unusual occurrence of synchysite-(Ce) in amygdales from  
533 the Esterel volcanic rocks, France: implications for rare-earth element mobility. *Can. Min.* 52, 837–  
534 856.

535 Bau, M., Dulski, P., 1995. Comparative study of yttrium and rare earth element behaviours in  
536 fluorine-rich hydrothermal fluids. *Contrib. Mineral. Petrol.* 119, 213–223.

- 537 Bau, M., Möller P., 1992. Rare earth element fractionation in metamorphogenic hydrothermal calcite,  
538 magnesite and siderite. *Mineral. Petrol.* 45, 231–246.
- 539 Bechstädt, T., Boni, M., 1994. Sedimentological, stratigraphical and ore deposits field guide of the  
540 autochthonous Cambro-Ordovician of Southwestern Sardinia. Servizio Geologico d'Italia, Roma,  
541 434 pp.
- 542 Belkin, H.E., De Vivo, B., Valera, R., 1984. Fluid inclusion study of some Sarrabus fluorite deposits,  
543 Sardinia, Italy. *Econ. Geol.* 79, 409–414.
- 544 Boni, M., Balassone, G., Fedele, L., Mondillo, N., 2009. Post-Variscan hydrothermal activity and ore  
545 deposits in southern Sardinia (Italy): selected examples from Gerrei (Silius Vein System) and  
546 Iglesias district. *Per. Miner.* 78, 19–35.
- 547 Boni, M., Rankin, A.H., Salvadori, M., 1990. Fluid inclusion evidence for the development of Zn-Pb-  
548 Cu-F skarn mineralisation in SW Sardinia (Italy). *Miner. Magazine* 54, 279–288.
- 549 Boni, M., Stein, H.J., Zimmerman, A., Villa, I.M., 2003. Re-Os age for molybdenite from SW  
550 Sardinia (Italy): A comparison with  $^{40}\text{Ar}/^{39}\text{Ar}$  dating of Variscan granitoids. *Mineral Exploration and*  
551 *Sustainable Development, Proceedings of the Seventh Biennial SGA Meeting on Mineral*  
552 *Exploration and Sustainable Development, Athens, Greece, 247–250.*
- 553 Bouabdellah, M., Banks, D., Klügel, A., 2010. Comments on “A late Triassic  $^{40}\text{Ar}/^{39}\text{Ar}$  age for the El  
554 Hammam high-REE fluorite deposit (Morocco): mineralization related to the Central Atlantic  
555 Magmatic Province?” by Cheilletz et al. (*Miner. Deposita* 45, 323–329, 2010). *Miner. Deposita* 45,  
556 729–731.
- 557 Brizzi, G., Olmi, F., Sabelli, C., 1994. Gli arseniati di Pira Inferida, Gonnosfanadiga (CA). *Rivista*  
558 *Mineralogica Italiana*, 3/1994, 193–206.

559 Brown, S.M., Fletcher, I.R., Stein, H.J., Snee, L.W., Groves, D.I., 2002. Geochronological  
560 constraints on pre-, syn-, and post-mineralization events at the world-class Cleo Gold Deposit,  
561 Eastern Goldfields Province, Western Australia. *Econ. Geol.* 97, 541–559.

562 Carmignani, L., Cortecci, G., Dessau, G., Duchi, G., Oggiano, G., Pertusati, P., Saitta, M., 1978. The  
563 antimony and tungsten deposit of Villasalto in South-Eastern Sardinia and its relationship with  
564 Hercynian tectonics. *Schweiz. mineral. petrogr. Mitt.* 58, 163–188.

565 Carmignani, L., Oggiano, G., Pertusati, P.C., 1994. Geological outlines of the Hercynian basement of  
566 Sardinia. In: *Petrology, geology and ore deposits of the Paleozoic basement of Sardinia, Guidebook*  
567 *to the B3 Field excursion, 16<sup>th</sup> General Meeting of the International Mineralogical Association, Pisa,*  
568 *pp 9–20.*

569 Carmignani, L., Oggiano, G., Barca, S., Conti, P., Salvadori, I., Eltrudis, A., Funedda, A., Pasci, S.,  
570 2001. *Geologia della Sardegna, Note illustrative della Carta Geologica della Sardegna alla scala*  
571 *1:200000. Mem. Descr. Carta Geologica d'Italia, Serv. Geol. It., 60, pp 283, Ist. Poligr. Zecca dello*  
572 *Stato, Roma.*

573 Castorina, F., Masi, U., Padalino, G., Palomba, M., 2008. Trace-element and Sr–Nd isotopic  
574 evidence for the origin of the Sardinian fluorite mineralization (Italy). *Appl. Geochem.* 23, 2906–  
575 2921.

576 Chakhmouradian, A.R., Wall, F., 2012. Rare Earth Elements: minerals, mines, magnets (and more).  
577 *Elements* 8, 333–342.

578 Chakhmouradian, A.R., Zaitsev, A.N., 2012. Rare Earth Mineralization in igneous rocks: sources and  
579 processes. *Elements* 8, 347–356.

580 Cheilletz, A., Gasquet, D., Filali, F., Archibald, D.A., Nespolo, M., 2010. A late Triassic  $^{40}\text{Ar}/^{39}\text{Ar}$   
581 age for the El Hammam high-REE fluorite deposit (Morocco): mineralization related to the Central  
582 Atlantic Magmatic Province? *Miner. Deposita* 45, 323–329.

583 Cook, N.J., Ciobanu, C.L., O’Rielly, D., Wilson, R., Das, K., Wade, B., 2013. Mineral chemistry of  
584 Rare Earth Element (REE) mineralization, Browns Ranges, Western Australia. *Lithos* 172-173, 192–  
585 213.

586 Crowley, Q.G., Floyd, P.A., Winchester, J.A., Franke, W., Holland, J.G., 2000. Early Paleozoic rift  
587 related magmatism in Variscan Europe: fragmentation of the Armorican Terrane Assemblage. *Terra*  
588 *Nova* 12, 171–180.

589 Di Vincenzo, G., Elter, F.M., Ghezzo, C., Palmeri, R., Ricci, C.A., 1994. Petrological evolution of  
590 the Palaeozoic basement of Sardinia. In: Carmignani, L., Ghezzo, C., Marcello, A., Pertusati, P.C.,  
591 Pretti, S., Ricci, C.A., Salvadori, I. (Eds): “Petrology, Geology and Ore Deposits of the Palaeozoic  
592 Basement of Sardinia”. *Guide Book to the Field Excursion*, 145, 643–658.

593 Dill, H.G., Hansen, B.T., Weber, B., 2011. REE contents, REE minerals and Sm/Nd isotopes of  
594 granite- and unconformity-related fluorite mineralization at the western edge of the Bohemian Massif:  
595 With special reference to the Nabburg-Wölsendorf District, SE Germany. *Ore. Geol. Rev.* 40, 132–  
596 148.

597 Förster, H.J., 2001. Synchysite-(Y) $\pm$ synchysite-(Ce) solid solutions from Markersbach, Erzgebirge,  
598 Germany: REE and Th mobility during high-T alteration of highly fractionated aluminous A-type  
599 granites. *Mineral. and Petrol.*, 72, 259–280.

600 Gaggero, L., Oggiano, G., Funedda, A., Buzzi, L., 2012. Rifting and arc-related early Paleozoic  
601 volcanism along the North Gondwana margin: geochemical and geological evidence from Sardinia  
602 (Italy). *J. Geol.* 120, 273–292.

603 Ghezzi, C., Orsini, J.B., 1982. Lineamenti strutturali e composizionali del batolite ercinico sardo-  
604 corso in Sardegna. In: Carmignani, L. et al. (Eds.): Guida alla Geologia del Paleozoico Sardo. Guide  
605 Regionali Soc. Geol. It., 165–181.

606 Gieré, R., 1996. Formation of rare earth minerals in hydrothermal systems. In: Jones, A. P., Wall, F.,  
607 Williams, C.T., (Eds.), Rare Earth Minerals: chemistry, origin and ore deposits, Mineralogical  
608 Society Series 7, Chapman and Hall, London, pp. 105–150.

609 Götze, J., 2012. Application of cathodoluminescence microscopy and spectroscopy in geosciences.  
610 *Microsc. Microanal.* 18, 1270–1284.

611 Gysi, A.P., Williams-Jones, A.E., 2013. Hydrothermal mobilization of pegmatite-hosted REE and Zr  
612 at Strange Lake, Canada: a reaction path model. *Geoch. Cosm. Acta* 122, 324–352.

613 Gysi, A.P., Williams-Jones, A.E., Harlov, D., 2015. The solubility of xenotime-(Y) and other HREE  
614 phosphates (DyPO<sub>4</sub>, ErPO<sub>4</sub> and YbPO<sub>4</sub>) in aqueous solutions from 100 to 250 °C and p<sub>sat</sub>. *Chem.*  
615 *Geol.* 401, 83–95.

616 Haack, U., Schnorrer-Köhler, G., Lüders, V., 1987. Seltene Erd-Mineralie aus hydrothermalen  
617 Gängen des Harzes. *Chem. Erde* 47, 41–45.

618 Kositsin, N., McNaughton, N.J., Griffin, B.J., Fletcher, I.R., Groves, D.I., Rasmussen, B., 2003.  
619 Textural and geochemical discrimination between xenotime of different origin in the Archaean  
620 Witwatersrand Basin, South Africa. *Geoch. Cosm. Acta* 67, 709–731.

621 Makin, S.A., Simandl, G.J., Marshall, D., 2014. Fluorite and its potential as an indicator mineral for  
622 carbonatite-related rare earth element deposits. In: Geological Fieldwork 2013, British Columbia  
623 Ministry of Energy and Mines, British Columbia Geological Survey Paper 2014-1, 207–212.

624 Migdisov, A.A., Williams-Jones A.E., 2014. Hydrothermal transport and deposition of the rare earth  
625 elements by fluorine-bearing aqueous liquids. *Miner. Deposita* 49, 987–997.

626 Möller, P., Bau M., 1993. Rare - earth patterns with positive cerium anomaly in alkaline waters from  
627 Lake Van, Turkey. *Earth Planet. Sci. Let.* 117, 671–676.

628 Möller, P., Giese, U., 1997. Determination of easily accessible metal fractions in rocks by batch  
629 leaching with acid cation – exchange resin. *Chem. Geol.* 137, 41 – 55.

630 Möller, P., Bau, M., Dulski, P., Lüders, V., 1998. REE and Y fractionation in fluorite and their  
631 bearing on fluorite formation. Proceedings of the 9<sup>th</sup> Quadrennial IAGOD Symp., Schweizerbart,  
632 Stuttgart, 575–592.

633 Möller, P., 1976. The application of Tb/Ca – Tb/La abundance ratios to problems of fluorspar genesis.  
634 *Miner. Deposita* 11, 111–116.

635 Möller, P., 1991. REE fractionation in hydrothermal fluorite and calcite. In: Pagel, M., Leroy, J.  
636 (Eds.), *Source, Transport and Deposition of Metals*. Balkema, Rotterdam, 91–94.

637 Möller, P., Franzke H.J., Lüders V., 1994. Post-orogene intraformationale Bildung der  
638 hydrothermalen Pb–Zn, F und F–Ba Lagerstätten im Schwarzwald. Technical report Mo 443/3 and Fr  
639 874/1, Intraformationale Lagerstättenbildung, GFZ-Postdam, Germany.

640 Möller, P., Morteani, G., Dulski, P., 1984. The origin of the calcites from Pb-Zn veins in the Harz  
641 Mountains, Federal Republic of Germany. *Chem. Geol.* 45, 91–112.

642 Muchez, P., Heijlen, W., Banks, D., Blundell, D., Boni, M., Grandia F., 2005. Extensional tectonics  
643 and the timing and formation of basin-hosted deposits in Europe. *Ore Geol. Rev.* 27, 241–267.

644 Muñoz, M., Boyce, A.J., Courjault-Radé, P., Fallick, A.E., Tollon, F., 1999. Continental basinal  
645 origin of ore fluids from southwestern Massif Central fluorite veins (Albigeois, France): evidence  
646 from fluid inclusion and stable isotope analyses. *Appl. Geochem.* 14, 447–458.

647 Muñoz, M., Premo, W.R., Courjault-Radé, P., 2005. Sm/Nd dating of fluorite from the worldclass  
648 Montroc fluorite deposit, southern Massif Central, France. *Miner. Deposita* 39, 970–975.

649 Natale, P., 1969. Il giacimento di Silius nel Gerrei. *Boll. Ass. Miner. Subalpina* 6, 1–35.

650 Oggiano, G., Gaggero, L., Funedda, A., Buzzi, L., Tiepolo, M., 2010. Multiple early Palaeozoic  
651 volcanic events at the northern Gondwana margin: U-Pb age evidence from the Southern Variscan  
652 branch (Sardinia, Italy). *Gondwana Res.* 17, 44–58.

653 Orlandi, P., Biagioni, C., Bindi, L., Nestola, F., 2014. Ichnusaite,  $\text{Th}(\text{MoO}_4)_2 \cdot 3\text{H}_2\text{O}$ , the first natural  
654 thorium molybdate: occurrence, description, and crystal structure. *Amer. Mineral.* 99, 2089–2094.

655 Orlandi, P., Gelosa, M., Bonacina, E., Caboni, F., Mamberti, M., Tanca, G., Vinci, A., 2013.  
656 Sardignaitite, gelosaitite et tancaite-(Ce): trois nouveaux minéraux de Su Seinargiu, Sarroch, Sardaigne,  
657 Italie. *Le Règne Minéral* 112, 39–52.

658 Samson, I.M., Wood, S.A., Finucane, K., 2004. Fluid inclusion characteristics and genesis of the  
659 fluorite-parisite mineralization in the Snowbird deposit, Montana. *Econ. Geol.* 99, 1727–1744.

660 Schaltegger, U., Pettke, T., Audétat, A., Reusser, E., Heinrich, C.A., 2005. Magmatic-to-  
661 hydrothermal crystallization in the W–Sn mineralized Mole Granite (NSW, Australia) Part I:  
662 Crystallization of zircon and REE-phosphates over three million years - a geochemical and U–Pb  
663 geochronological study. *Chem. Geol.* 220, 215–235.

664 Schwinn, G., Markl, G., 2005. REE systematics in hydrothermal fluorite. *Chem. Geol.* 216, 225–248.

665 Stara, P., Rizzo, R., Tanca, G.A., 1996. Iglesiasite e Arburese. *Miniere e Minerali. Ente Minerario*  
666 *Sardo* 2, 192 pp.

667 Subías, I., Fernández-Nieto, C., 1995. Hydrothermal events in the Valle de Tena (Spanish Western  
668 Pyrenees) as evidenced by fluid inclusions and trace-element distribution from fluorite deposits.  
669 *Chem. Geol.* 124, 267–282.

670 Taylor, St.R., McLennan, S.M., 1985. *The continental crust: its composition and evolution.*  
671 Blackwell Scientific Publications Oxford, London, Edinburgh, 312 pp.

672 Valera, R., 1974. Appunti sulla morfologia, termometria e composizione delle inclusioni fluide di  
673 fluoriti sarde. *Rend. Soc. It. Min. Petr.* 30, 459–480.

674 Von Gehlen, K., Grauert, B., Nielsen, H., 1986. REE minerals in southern Schwarzwald veins and  
675 isotope studies on gypsum from the central Schwarzwald, F.R. Germany. *N. Jb. Miner. Mh.* 9, 393–  
676 399.

677 Williams-Jones, A.E., Samson, I.M., Olivo, G.R., 2000. The genesis of hydrothermal fluorite-REE  
678 deposits in the Gallinas Mountains, New Mexico. *Econ. Geol.* 95, 327–342.

679 Williams-Jones, A.E., Migdisov, A.A., Samson, I.M., 2012. Hydrothermal mobilization of the rare  
680 earth elements - a tale of “Ceria” and “Yttria”. *Elements*, 8, 355–360.

681

## 682 **Figures captions**

683 Figure 1. A) Major tectonic and metamorphic zones of the Hercynian basement in Sardinia (Italy)  
684 (Carmignani et al., 1991, modified); yellow star = Silius area. B) Geological sketch map of the Silius  
685 area (Nuova Mineraria Silius s.p.a., modified).

686

687 Figure 2. A) Silius Mine - production gallery at 235 m a.s.l.: ribbon structure (fluorite, calcite, galena)  
688 of the San Giuseppe vein (Boni et al., 2009, modified). B) Green-purple banded fluorite of the San  
689 Giorgio vein. C) & D) San Giuseppe vein (zoned fluorite, calcite/dolomite, galena) cutting and partly  
690 replacing the San Giorgio vein: chalcedony-rich fragments of the San Giorgio vein occur as breccia  
691 clasts cemented by San Giuseppe calcite (Boni et al., 2009, reinterpreted).

692

693 Figure 3. A) & B) First fluorite generation, luminescing blue under CL. C) & D) Cubic crystal of the  
694 second fluorite generation in carbonate gangue: calcite (yellow-orange under CL) is replaced by  
695 dolomite (dark under CL). E) & F) Third fluorite generation consisting of microcrystals associated  
696 with quartz and barite in a veinlet, cutting the carbonate gangue (dark-reddish under CL).

697

698 Figure 4. A) Fe-bearing dolomite crystal showing a mottled texture. B) Calcite replaced by dolomite,  
699 which locally reaches ankerite composition. C) & D) Acicular and tabular crystals of synchysite  
700 irregularly distributed throughout the dolomite, Fe-bearing dolomite and ankerite gangue. E) Acicular  
701 crystals of synchysite within quartz veinlets and in cavities between calcite and dolomite. F)  
702 Synchysite across dolomitized calcite, quartz and fluorite of the third generation. G) Synchysite  
703 aggregate of crystals, clearly cemented by fluorite. H) Subhedral crystal of xenotime cutting across  
704 calcite and dolomite. Backscattered images (BSE) from SEM-EDS.

705

706 Figure 5. Dolomite and Fe-bearing dolomite chemical compositions plotted in the  $\text{CaMg}(\text{CO}_3)_2$ -  
707  $\text{CaFe}(\text{CO}_3)_2$ - $\text{CaMn}(\text{CO}_3)_2$  diagram (EDS analyses).

708

709 Figure 6. A) REE concentrations in fluorite bulk samples, normalized to PAAS (post-Archean  
710 Australian Shale; Taylor and McLennan, 1985). B) REE concentrations in carbonate gangue bulk  
711 samples, normalized to PAAS. C) REE concentrations in host rock samples, normalized to PAAS.  
712 ICP-OES-MS analyses.

713

714 Figure 7. Y/Ho vs. La/Ho in bulk samples of fluorite. Two samples are clearly contaminated by  
715 carbonates (see Table 2).

716

717 Table 1 - Major (wt.%) and minor (ppm) elements compositions of Silius fluorite (ICP-OES-MS on  
718 bulk sample).

719 Table 2 - Major (wt.%) and minor (ppm) elements compositions of the carbonate gangue of Silius  
720 veins (ICP-OES-MS on bulk samples).

721 Table 3 - Chemical compositions of synchysite in the Silius veins.

722 Table 4 - Major (wt.%) and minor (ppm) elements compositions of Silius host rocks (ICP-OES-MS  
723 on bulk samples).

724

725 Table A1 - Description of the analyzed samples from the Silius vein system.

726 Table A2 - Chemical composition of standards used for WDS analysis of synchysite-(Ce).